

Insights into the nature of plume-ridge interaction and outflux of H₂O from the Galápagos Spreading Centre

M. L. M. Gleeson^{1,2}, S. A. Gibson¹

¹Department of Earth Sciences, University of Cambridge, Downing Street, Cambridge, CB2 3EQ, UK.

²School of Earth and Environmental Sciences, Cardiff University, Park Place, Cardiff, CF10 3AT, UK.

Contents of this file

1. The effect of secondary processes on the volatile contents of MORB.
2. Mantle melting models.
3. Additional figures (Fig. S.1 - S.15)

Additional Supporting Information (available via:

<https://zenodo.org/badge/latestdoi/379869011>

1. Excel spreadsheet of glass compositions and Jupyter Notebook containing the necessary code to reproduce the along-ridge calculations.

Corresponding author: M. L. M. Gleeson, School of Earth and Ocean Sciences, Cardiff University, Park Place, Cardiff, CF10 3AT, UK (gleesonm1@cardiff.ac.uk)

1. The effect of secondary processes on the volatile contents of MORB

Secondary processes play an important role in controlling the volatile content of basaltic glasses (Dixon, 1997; Kendrick et al., 2015). For example, basaltic glasses analysed from subaerial eruptions have generally lost some of the originally dissolved H₂O and CO₂ due to the low solubility of these volatiles at atmospheric pressure (Dixon, 1997). One way around this is to analyse the volatile contents of basaltic glasses erupted on the ocean floor, beneath 1-3 km of water (Peterson et al., 2017). The elevated pressure of eruption (due to the overlying water column) may cause most of the originally dissolved magmatic H₂O to remain dissolved in the magma during eruption, even if the CO₂ is lost at much greater pressures. However, the volatile contents of ocean floor basalts are commonly influenced by assimilation of seawater and/or hydrothermal brines (Kendrick et al., 2015). Below, we investigate the influence of both of these processes on the H₂O contents of the GSC basalts.

1.1. Degassing

Whilst CO₂ measurements were not made in this study due to constraints on analytical time, CO₂ analyses of basaltic glasses from the GSC were carried out by Cushman, Sinton, Ito, and Dixon (2004). Their results indicate that the GSC samples have degassed a significant proportion of their CO₂. Additionally, while the solubility of H₂O is much higher than that of CO₂ in basaltic magmas, it is still important to consider the influence that degassing of a mixed H₂O-CO₂ fluid may have on the H₂O contents of the GSC basalts.

In open-system degassing, where the fluid phase chemically separates from the melt and equilibrium between the melt and fluid is not maintained, the fluid phase is composed almost entirely of CO₂ and no H₂O is lost from the system. On the other hand, in closed-system degassing, where chemical equilibrium between the fluid and melt phase is maintained during ascent, a substantial amount of H₂O may be lost. It is therefore necessary to evaluate whether open- or closed-system degassing is most likely, and the maximum influence that closed-system degassing may have on the H₂O content of the GSC basalts.

In several regions of OIB melt generation (e.g. Samoa, Pitcairn, Hawaii, Society Islands) near vertical trends in H₂O - CO₂ space have been used as evidence that open-system degassing dominates (Dixon, 1997; Workman et al., 2006; Kendrick et al., 2014). Unfortunately, due to the diverse geochemical enrichment displayed by the GSC basalts, and the limited number of CO₂ analyses that exist, it is not possible to say for certain that open-system degassing dominates the GSC volatiles. Therefore, we used the latest version of the MELTS thermodynamic algorithms, with updated H₂O and CO₂ solubility models (rhyoliteMELTS v1.2.0; Ghiorso and Gualda (2015)) to evaluate the extent of H₂O loss that may occur due to closed system degassing (Fig. S2). To do so, a series of polybaric degassing models were run in which the initial CO₂ content was set at 239 times the Nb content of the GSC basalt under consideration (Saal et al., 2002), and the initial H₂O content was iteratively varied until the degassing path passes through the composition of the chosen GSC basalt under consideration in H₂O-CO₂ space.

The extent of H₂O loss predicted is dependent on the degree of enrichment of the GSC basalt under consideration. Most D-MORBs and N-MORBs display a maximum H₂O loss

of <0.5% of their original H₂O content, and many of the E-MORBs display a maximum H₂O loss of 2% or less (Fig. S2). The largest H₂O loss that is predicted by this modelling (5%) occurs for sample 17D-4, the most enriched sample under consideration. The extent of H₂O loss is, however, dependent on the initial CO₂ concentration chosen. Unfortunately, the initial CO₂ contents, and CO₂/Nb and CO₂/Ba ratios, of the GSC basalts are poorly constrained. Nevertheless, while other estimates for the CO₂/Nb or CO₂/Ba ratio of primary mantle melts beneath the GSC could be used in these calculations (Miller et al., 2019), the maximum amount of H₂O degassing remains low ($\ll 10\%$), even for the most enriched GSC basalts. Since the influence of closed-system degassing on the H₂O content of the GSC basalts appears to be relatively minor, and represents the maximum amount of H₂O that may have been lost from these basalts, we suggested that degassing does not play an important role in controlling the H₂O contents of the GSC basalts.

1.2. Brine assimilation

During mantle melting, Cl and K are both highly incompatible and, as a result, the Cl/K ratios of basaltic magmas should be independent of the degree of melting (Saal et al., 2002; Kendrick et al., 2015). The primary Cl/K ratio of OIB and MORB magmas is typically placed at 0.01 - 0.08, although values up to 0.15 have been suggested in certain locations (Michael & Cornell, 1998; Hanyu et al., 2019). Scatter in the Cl/K ratio of MORBs or OIBs is, therefore, commonly attributed to the assimilation of Cl-rich material, such as a brine (Kendrick et al., 2015).

Almost all of the GSC basalts analysed in this study, and that of Ingle et al. (2010), have Cl/K ratios that are significantly higher than 0.08, which clearly indicates that assimilation of a Cl-rich component has occurred. Kendrick et al. (2015) showed that

assimilation of even very concentrated brines (~ 55 wt% NaCl) may contribute up to 30% of the measured H₂O in submarine lavas from Samoa. As a result, it is important to constrain the influence that this assimilation process may have on the H₂O content of the GSC basalts. If the H₂O/Cl ratio of the assimilated component and the extent of Cl that has been assimilated by the GSC basalts can be estimated, it is possible to determine the amount of H₂O that has been assimilated by each sample prior to eruption. This can be achieved using the observed correlations between H₂O/Cl and K/Cl or F/Cl (Fig. S3).

Assuming that the assimilated brine component has a K/Cl or F/Cl ratio <0.0001 (Kendrick et al., 2015), the H₂O/Cl content of the assimilated brine can be estimated by calculating the y-intercept of the regression lines between H₂O/Cl and K/Cl or F/Cl (Fig. S3). The calculated H₂O/Cl ratios of the assimilated component estimated from these two graphs are within error of each other (-0.52 ± 3.25 and 0.61 ± 2.68 , respectively). The very low values estimated indicate that the assimilated component likely represents a very concentrated brine, with $>55\%$ NaCl (Kendrick et al., 2015). Using a H₂O/Cl ratio of 0.61 for the assimilated brine, the amount of H₂O assimilated by each of the GSC basalts can be estimated by calculating the amount of Cl assimilated (that is, the concentration of Cl required to reduce the Cl/K ratio to 0.08). This analysis indicates that the GSC basalts have assimilated between 0 and 0.2 wt% H₂O, which has a substantial influence on their H₂O/La ratios (>50) of some of the isotopically depleted GSC basalts. All of our interpretations of mantle source H₂O contents made in the main text are based on H₂O measurements that have been corrected for the influence of brine assimilation.

2. Mantle Melting Models

In this study, we use the pymelt module of Matthews, Shorttle, and Wong (2020) to model adiabatic decompression melting of a lithologically heterogeneous mantle (lherzolite-pyroxenite; using parameterisations of lherzolite and silica-undersaturated pyroxenite melting from Matthews, Wong, Shorttle, Edmonds, and MacLennan (2021)). At present, pymelt calculates the melt fraction versus depth curves for the different mantle lithologies as a function of the mantle potential temperature and the proportion of the different components in the source (i.e. lherzolite, pyroxenite and harzburgite; Fig. S5). However, these calculations cannot, by themselves, constrain the trace element composition of the melts formed during adiabatic decompression melting. To get at that information, we require knowledge of the mineralogy of the different source components and a framework to determine how the composition of the pooled melt phase will be influenced by changes in mantle flow velocity (owing to buoyant, plume-driven upwelling) and the contribution of channelised, plume-derived melts.

2.1. Source mineralogy

In previous studies, the mineralogy of the source has typically been determined using experimentally constrained 'melting equations' (e.g., descriptions of the change in mineral proportions with increasing melt fraction; Gleeson, Gibson, and Williams (2020)) or the MELTS thermodynamic algorithm (Lambart, 2017). However, melting equations do not contain information about how the mineral proportions may change with pressure as well as melt fraction, a critical factor during adiabatic decompression melting.

As a result, we opt to follow the thermodynamic approach for estimating the mineralogy of the different mantle components. Specifically, in this study we use PerpleX

alongside the recent thermodynamic dataset of Holland, Green, and Powell (2018), and the solubility models for olivine, clinopyroxene, orthopyroxene, garnet, spinel, plagioclase, and melt from Jennings and Holland (2015), to model the mineralogical properties of the various mantle component in the KNMASTOCr system (Connolly, 2009) (Fig. S6 & S7. The modal mineralogy of the various mantle components during adiabatic decompression melting is then determined as a function of pressure and melt fraction using these PerpleX simulations (Fig. S8).

Using this approach, we can compare the various partitioning behaviours of key volatile and non-volatile trace elements during melting of the different mantle components. When we do so, we find that H₂O displays very similar partitioning behaviour to La during melting of a lherzolitic mantle component until very low pressures (trace element partitioning is taken from Gibson and Geist (2010) and H₂O partitioning is taken from Rosenthal, Hauri, and Hirschmann (2015); Fig. S9). The relative compatibility of H₂O compared to La and Ce at <1 GPa results from the greater partitioning of H₂O in orthopyroxene compared to these trace elements, but has little influence on the overall partitioning behaviour of H₂O during mantle melting as >99% of the H₂O contained within a mantle source will enter the melt phase at higher pressures (i.e. a low melt fractions). Notably, our model results also demonstrate that H₂O is likely less compatible than La during melt of a pyroxenitic source component (using the experimental partitioning data from Rosenthal et al. (2015); Fig. S9).

If we consider the partitioning behaviour of F, we find that it displays similar compatibility to Nd during melting of a lherzolitic source component, but is slightly less compatible than Nd during melting of a pyroxenitic lithology (F partitioning data from

Dalou, Koga, Shimizu, Boulon, and Devidal (2012); Fig. S9). Other interesting features that can be observed in these calculations is the compatibility of the heavy REE during high pressure melting of a pyroxenitic lithology ($D > 1$) owing to the large proportion of garnet in the pyroxenitic source ($\sim 2\%$).

2.2. Calculating melt compositions

Once the mineralogy of the source components undergoing adiabatic decompression melting have been determined, the trace element composition of the pooled melt phase can easily be calculated. To determine the composition of the melt phase produced by decompression melting beneath a ridge axis we use first calculate the melts that are formed at each pressure within the melting region. For most of our calculations, we consider pressure steps of 10 MPa, and calculate the trace element composition of the melts produced at these pressure intervals using a non-modal batch melting equation:

$$\frac{C_l}{C_o} = \frac{1}{D + F * (1 - P)}$$

where C_l represents the concentration of some trace element in the melt ; C_o represents the concentration in the initial solid assemblage; F is the instantaneous melt fraction formed; D is the partition coefficient weighted by the proportion of each mineral in the solid assemblage; and P represents the partition coefficient of each mineral weighted by the contribution of that mineral to the melt phase (not it's original proportion). The composition of the residue at each step is calculated using a mass balance approach, and this value is taken forward as the 'source' composition for the melting calculation at the next pressure step.

Second, we calculate the accumulated melts that form from each parcel of mantle residue that is exiting the melting region. In other words, for each depth interval within the melting region we calculate the aggregated melt composition for melting to that pressure. This is displayed in Fig. S10 where the blue dots represent the locations where the melt composition is calculated for a single parcel of mantle moving through the melting region:

$$C_{column}^{P_i} = \sum_{j=0}^i C_j^{P_j} * Frac^j$$

where $C_j^{P_j}$ represents the composition of the melt produced at location j (or pressure P_j) in the melt column, and $Frac^j$ represents the fraction of melt produced at pressure P_j relative to the total melt fraction of that source component at pressure P_i .

We then calculate the composition of the aggregated pooled melt at the ridge axis by summing the composition of aggregated melts formed at each pressure interval in the melt column weighted by their contribution to the final pooled melt phase. This weighting factor is determined by multiplying the total melt fraction of the source component at each depth interval with the relative lateral flow velocity of material exiting the melting region (U_r), i.e., $\omega^{P_i} = (U_r^{P_i} * F^{P_i}) / (\sum_{j=0}^n U_r^{P_j} * F^{P_j})$. In this way, we are able to account for the influence of buoyant, plume-driven upwelling. Notably, our approach is consistent with previous studies that have considered the nature of plume-ridge interaction in the Galápagos (Ingle et al., 2010).

$$C_{lith_1} = \sum_{i=0}^n \omega^{P_i} * C_{column}^{P_i}$$

This calculation is performed for all lithologies and the final aggregated melt can then be calculated via:

$$C_{final} = P_d * C_{Lhz} + (1 - Pd) * C_{Pyx}$$

where P_d represents the proportion of material derived from the depleted/herzolitic component and is calculated via:

$$P_d = \sum_{i=0}^n \omega^{P_i} * (F_{Lhz}^{P_i} * X_d) / (F_{Lhz}^{P_i} * X_d + F_{Pyx}^{P_i} * (1 - X_d))$$

where X_d represents the mass.

In a similar manner, the crustal thickness produced by melting beneath the ridge axis can be calculated by summing the volume of melt produced at each depth in the melting region per unit time (i.e accounting for changes in the relative flow velocity of material leaving the melting zone):

$$Crustal\ Thickness = \sum_{i=0}^n (\rho_{solid}^{P_i} / \rho_{liquid}) * F_{total}^{P_i} * U_r^{P_i} * \delta h$$

where δh represents the height (in m) between each calculation step in the melting region and $\rho_{solid}^{P_i}$ represents the mean density of the solid components weighted by their contribution to the melt phase. Here we assume that $\rho_{Pyx} = 3400\ kg.m^{-3}$, $\rho_{Lhz} = 3300\ kg.m^{-3}$ and $\rho_{melt} = 2900\ kg.m^{-3}$.

The composition of channelised, volatile-rich melts formed in the Galápagos plume stem is calculated as the aggregated melt formed by incremental batch melting at $\sim 10\ MPa$ intervals between the initiation of melting and the pressure of channel formation.

References

- Connolly, J. (2009). The geodynamic equation of state: what and how. *Geochemistry, Geophysics, Geosystems, 10*(10).
- Cushman, B., Sinton, J., Ito, G., & Dixon, J. E. (2004). Glass compositions, plume-ridge interaction, and hydrous melting along the galápagos spreading center, 90.5 w to 98 w. *Geochemistry, Geophysics, Geosystems, 5*(8).
- Dalou, C., Koga, K. T., Shimizu, N., Boulon, J., & Devidal, J.-L. (2012). Experimental determination of f and cl partitioning between lherzolite and basaltic melt. *Contributions to Mineralogy and Petrology, 163*(4), 591–609.
- Dixon, J. E. (1997). Degassing of alkalic basalts. *American Mineralogist, 82*(3-4), 368–378.
- Ghiorso, M. S., & Gualda, G. A. (2015). An h 2 o-co 2 mixed fluid saturation model compatible with rhyolite-melts. *Contributions to Mineralogy and Petrology, 169*(6), 1–30.
- Gibson, S., & Geist, D. (2010). Geochemical and geophysical estimates of lithospheric thickness variation beneath galápagos. *Earth and Planetary Science Letters, 300*(3-4), 275–286.
- Gleeson, M. L., Gibson, S. A., & Williams, H. M. (2020). Novel insights from fe-isotopes into the lithological heterogeneity of ocean island basalts and plume-influenced morbs. *Earth and Planetary Science Letters, 535*, 116114.
- Hanyu, T., Shimizu, K., Ushikubo, T., Kimura, J.-I., Chang, Q., Hamada, M., ... Ishikawa, T. (2019). Tiny droplets of ocean island basalts unveil earth's deep chlorine cycle. *Nature communications, 10*(1), 60.

- Harpp, K. S., & White, W. M. (2001). Tracing a mantle plume: Isotopic and trace element variations of galápagos seamounts. *Geochemistry, Geophysics, Geosystems*, 2(6).
- Holland, T. J., Green, E. C., & Powell, R. (2018). Melting of peridotites through to granites: a simple thermodynamic model in the system kncfmashtocr. *Journal of Petrology*, 59(5), 881–900.
- Ingle, S., Ito, G., Mahoney, J. J., Chazey, W., Sinton, J., Rotella, M., & Christie, D. M. (2010). Mechanisms of geochemical and geophysical variations along the western galápagos spreading center. *Geochemistry, Geophysics, Geosystems*, 11(4).
- Jennings, E. S., & Holland, T. J. (2015). A simple thermodynamic model for melting of peridotite in the system ncfmasocr. *Journal of Petrology*, 56(5), 869–892.
- Kendrick, M. A., Jackson, M. G., Hauri, E. H., & Phillips, D. (2015). The halogen (f, cl, br, i) and h₂o systematics of samoan lavas: Assimilated-seawater, em2 and high-3he/4he components. *Earth and Planetary Science Letters*, 410, 197–209.
- Kendrick, M. A., Jackson, M. G., Kent, A. J., Hauri, E. H., Wallace, P. J., & Woodhead, J. (2014). Contrasting behaviours of co₂, s, h₂o and halogens (f, cl, br, and i) in enriched-mantle melts from pitcairn and society seamounts. *Chemical Geology*, 370, 69–81.
- Lambart, S. (2017). No direct contribution of recycled crust in icelandic basalts. *Geochimical Perspectives Letters*.
- Le Voyer, M., Hauri, E. H., Cottrell, E., Kelley, K. A., Salters, V. J., Langmuir, C. H., ... Füri, E. (2019). Carbon fluxes and primary magma co₂ contents along the global mid-ocean ridge system. *Geochemistry, Geophysics, Geosystems*, 20(3), 1387–1424.

- Matthews, S., Shorttle, O., & Wong, K. (2020). pymelt: First release. *Geochemistry, Geophysics, Geosystems*.
- Matthews, S., Wong, K., Shorttle, O., Edmonds, M., & Maclennan, J. (2021). Do olivine crystallization temperatures faithfully record mantle temperature variability? *Geochemistry, Geophysics, Geosystems*, 22(4), e2020GC009157.
- Michael, P. J., & Cornell, W. C. (1998). Influence of spreading rate and magma supply on crystallization and assimilation beneath mid-ocean ridges: Evidence from chlorine and major element chemistry of mid-ocean ridge basalts. *Journal of Geophysical Research: Solid Earth*, 103(B8), 18325–18356.
- Miller, W. G., Maclennan, J., Shorttle, O., Gaetani, G. A., Le Roux, V., & Klein, F. (2019). Estimating the carbon content of the deep mantle with icelandic melt inclusions. *Earth and Planetary Science Letters*, 523, 115699.
- Peterson, M., Saal, A., Kurz, M., Hauri, E., Blusztajn, J., Harpp, K., ... Geist, D. (2017). Submarine basaltic glasses from the galapagos archipelago: determining the volatile budget of the mantle plume. *Journal of Petrology*, 58(7), 1419–1450.
- Rosenthal, A., Hauri, E., & Hirschmann, M. (2015). Experimental determination of c, f, and h partitioning between mantle minerals and carbonated basalt, co₂/ba and co₂/nb systematics of partial melting, and the co₂ contents of basaltic source regions. *Earth and Planetary Science Letters*, 412, 77–87.
- Rudge, J. F., Maclennan, J., & Stracke, A. (2013). The geochemical consequences of mixing melts from a heterogeneous mantle. *Geochimica et Cosmochimica Acta*, 114, 112–143.
- Saal, A. E., Hauri, E. H., Langmuir, C. H., & Perfit, M. R. (2002). Vapour undersatu-

- ration in primitive mid-ocean-ridge basalt and the volatile content of earth's upper mantle. *Nature*, 419(6906), 451.
- Shishkina, T., Botcharnikov, R., Holtz, F., Almeev, R., & Portnyagin, M. V. (2010). Solubility of h₂o-and co₂-bearing fluids in tholeiitic basalts at pressures up to 500 mpa. *Chemical geology*, 277(1-2), 115–125.
- Workman, R. K., Hauri, E., Hart, S. R., Wang, J., & Blusztajn, J. (2006). Volatile and trace elements in basaltic glasses from samoa: Implications for water distribution in the mantle. *Earth and Planetary Science Letters*, 241(3-4), 932–951.

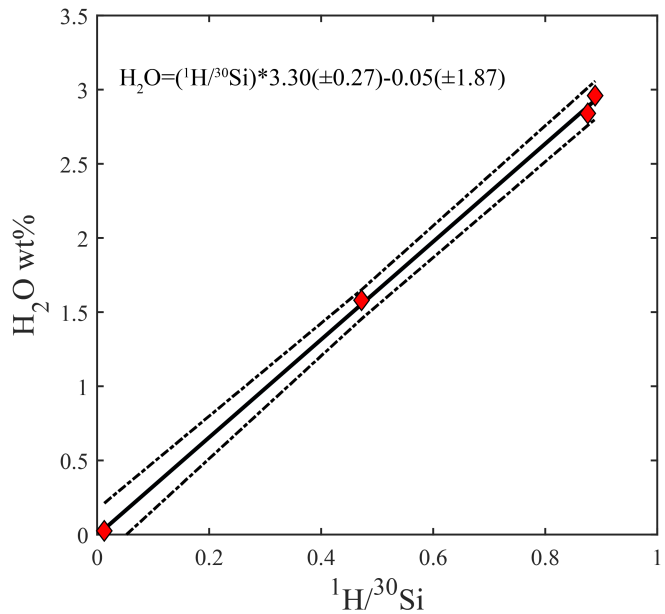


Figure S1. H_2O calibration line for SIMS analyses in this study. Standard values taken from Shishkina et al. (2010).

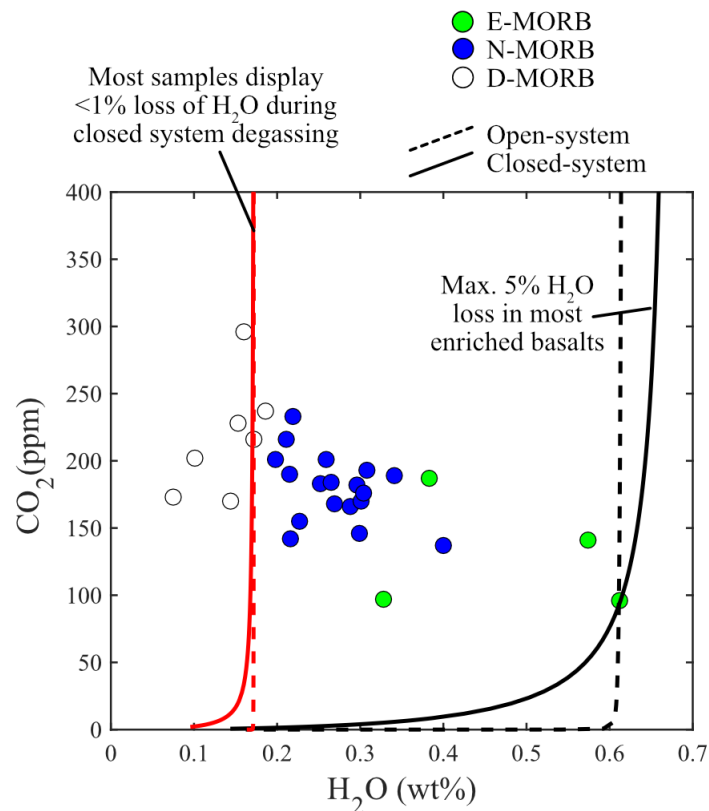


Figure S2. $\text{H}_2\text{O}-\text{CO}_2$ degassing paths and isobars are calculated using MagmaSat (Ghiorso & Gualda, 2015). Red isobars are calculated for an enriched GSC basalt (17D-4) and the grey isobars are calculated for a more depleted GSC basalt (63D-1). Red and black lines show the degassing path for these two GSC samples. Data from Cushman et al. (2004).

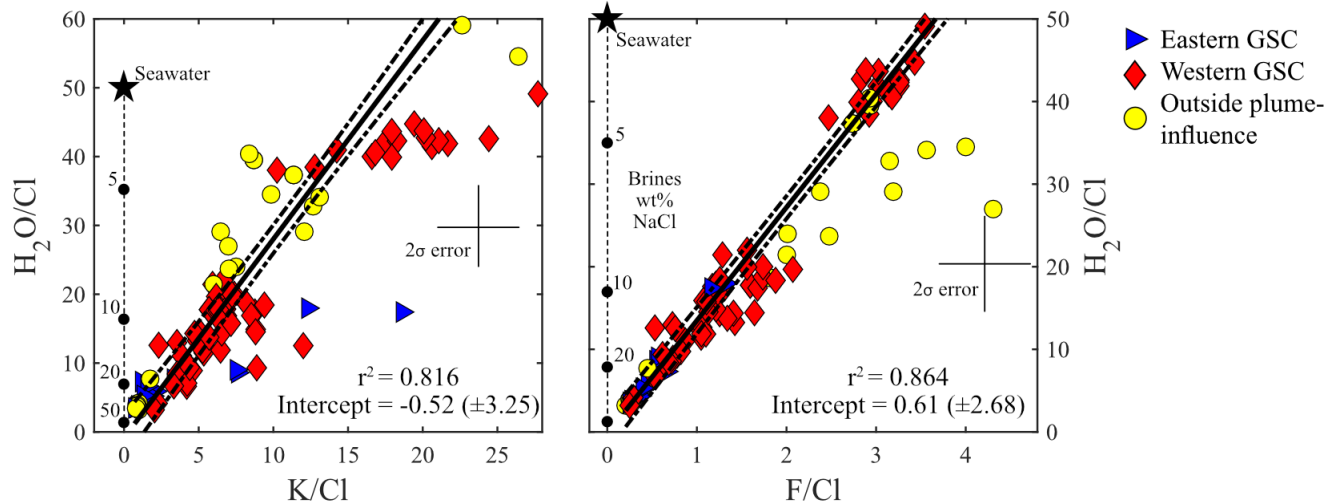


Figure S3. Correlation between H₂O/Cl and **A.** K₂O/Cl or **B.** F/Cl (data from outside the region of plume influence is not included in the correlations). Y-intercepts can be used to estimate the H₂O/Cl content of the assimilated component. Data from the eastern GSC is from this study and Le Voyer et al. (2019). Data from the western GSC is from Cushman et al. (2004); Ingle et al. (2010); Le Voyer et al. (2019). The composition of seawater and brines is taken from Kendrick et al. (2015).

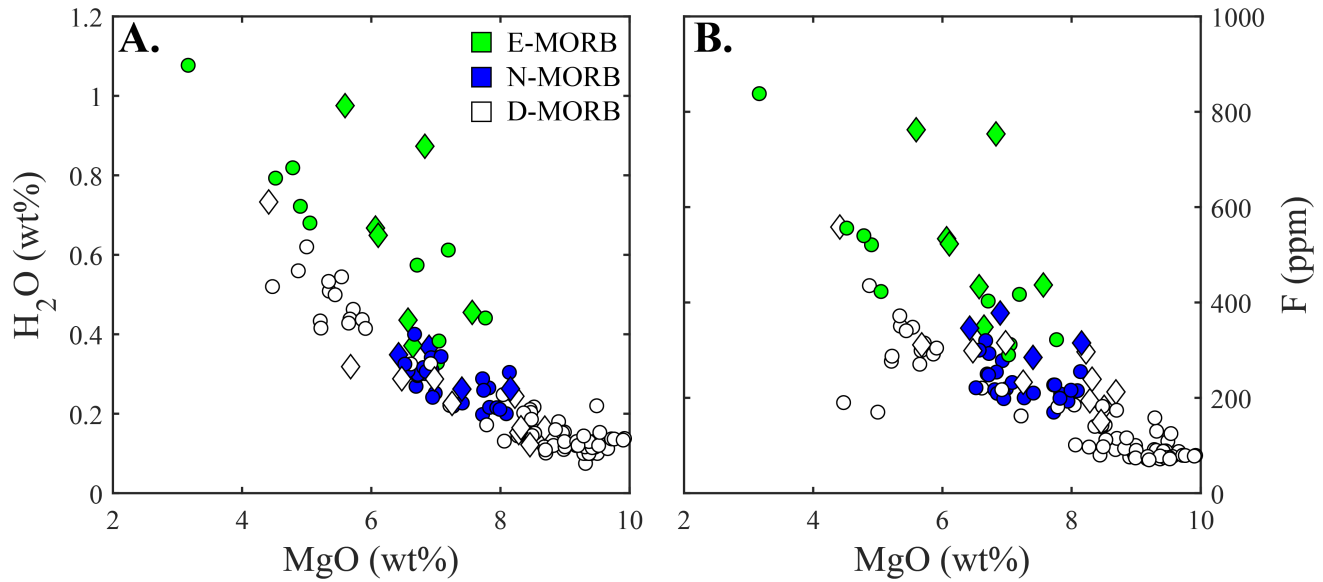


Figure S4. Harker diagrams showing the relationship between MgO and the volatile contents of the GSC basalts (H_2O and F). Data from this study is displayed by diamond symbols and published data by circular symbols (Cushman et al., 2004; Ingle et al., 2010). GSC E-MORBs clearly have higher H_2O and F concentrations compared to N-MORBs and D-MORBs at a given MgO content. The data displayed here has not been corrected for the influence of brine assimilation.

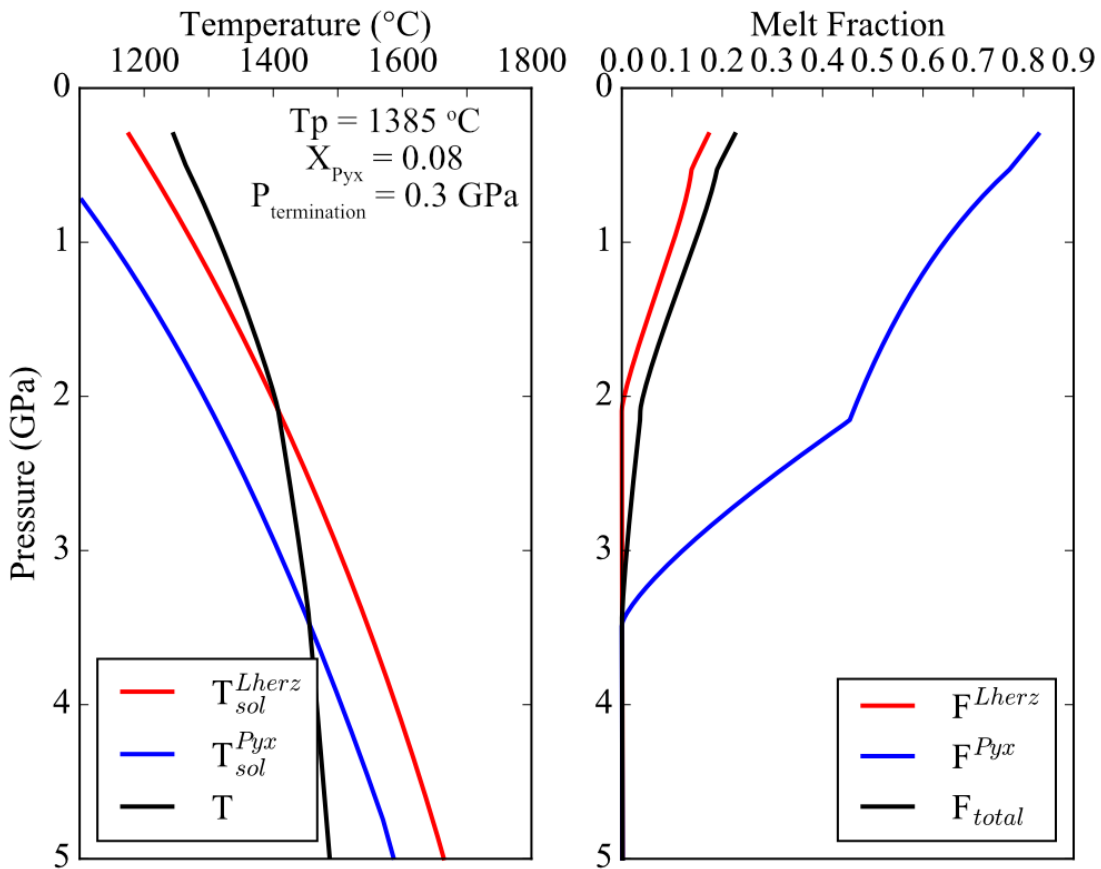


Figure S5. Melt fraction versus depth curves and P - T paths for mantle melting beneath the easter GSC at $\sim 90.5^{\circ}\text{W}$. Parameters used in these calculations are also present in Table 1 of the main text. Only subtle differences are present in the models used to recreate the geochemical signatures of basalts from the eastern and western GSC. Calculations are performed using the pymelt modules (Matthews et al., 2020)

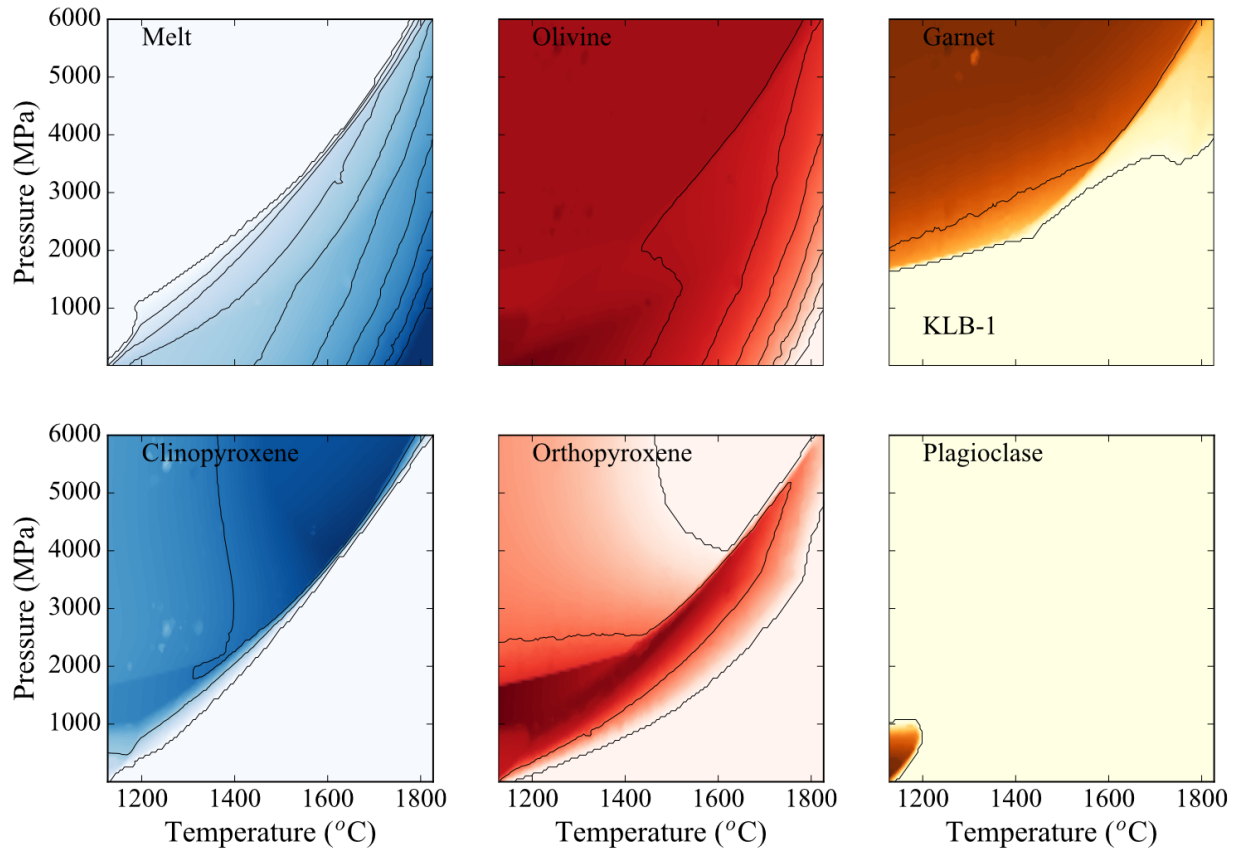


Figure S6. Mineral proportions for the KLB-1 lherzolite predicted by PerpleX.

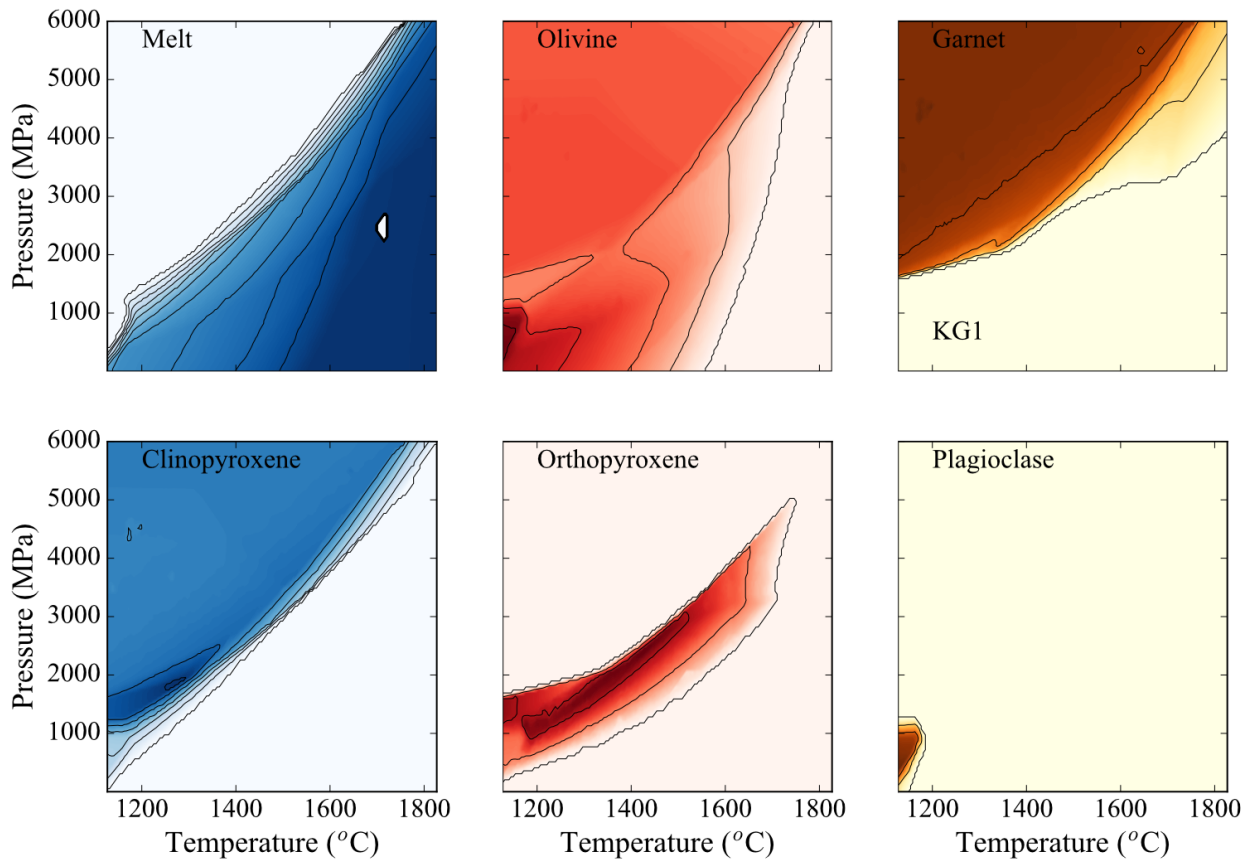


Figure S7. Mineral proportions for the KG1 pyroxenite predicted by PerpleX.

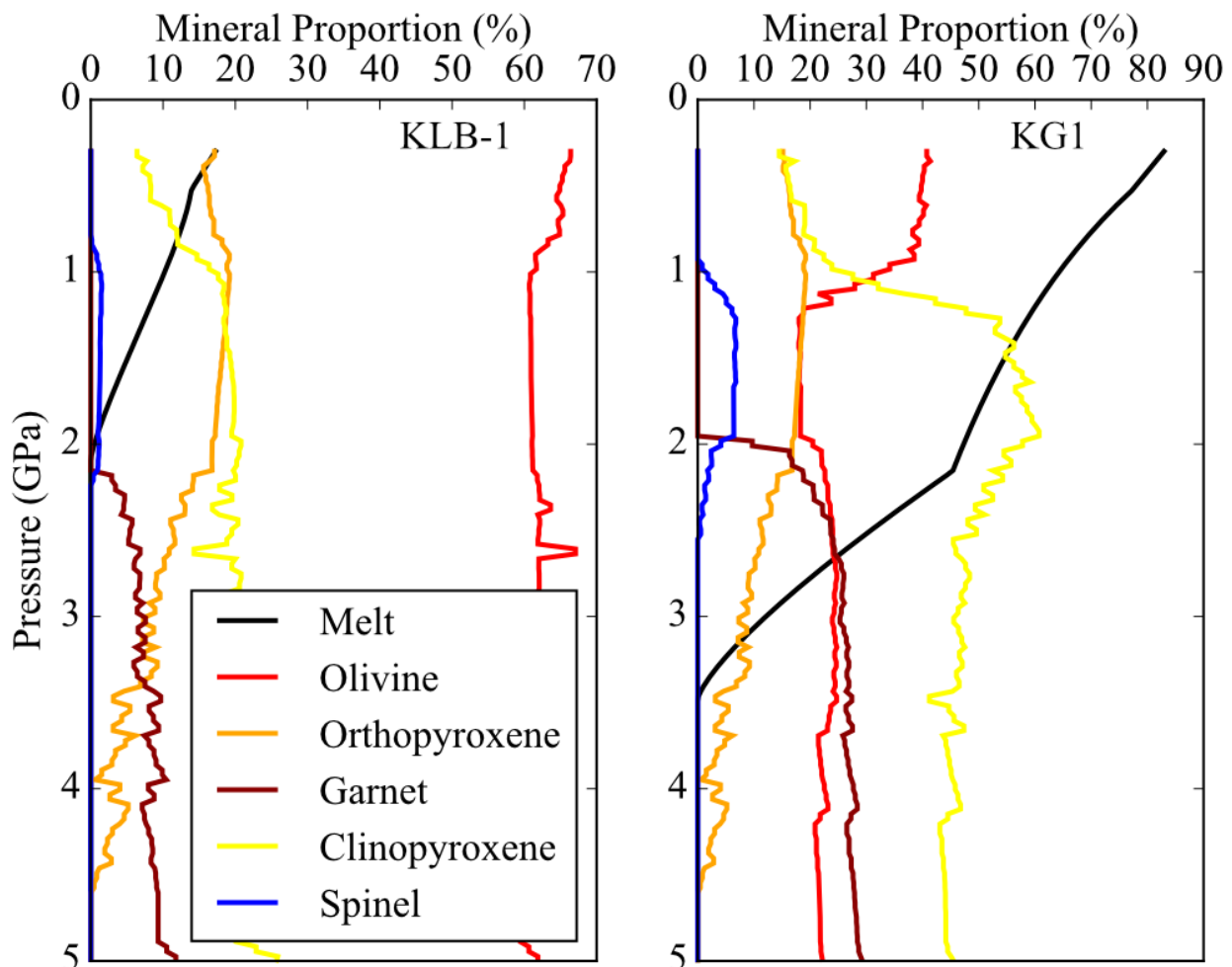


Figure S8. Mineral proportions predicted for the KLB-1 lherzolite and the KG1 peridotite during adiabatic decompression melting. Mineral proportions extracted from PerpleX calculations and the P-T path of the mantle and the melt fraction of each component is calculated using pymelt (Matthews et al., 2020).

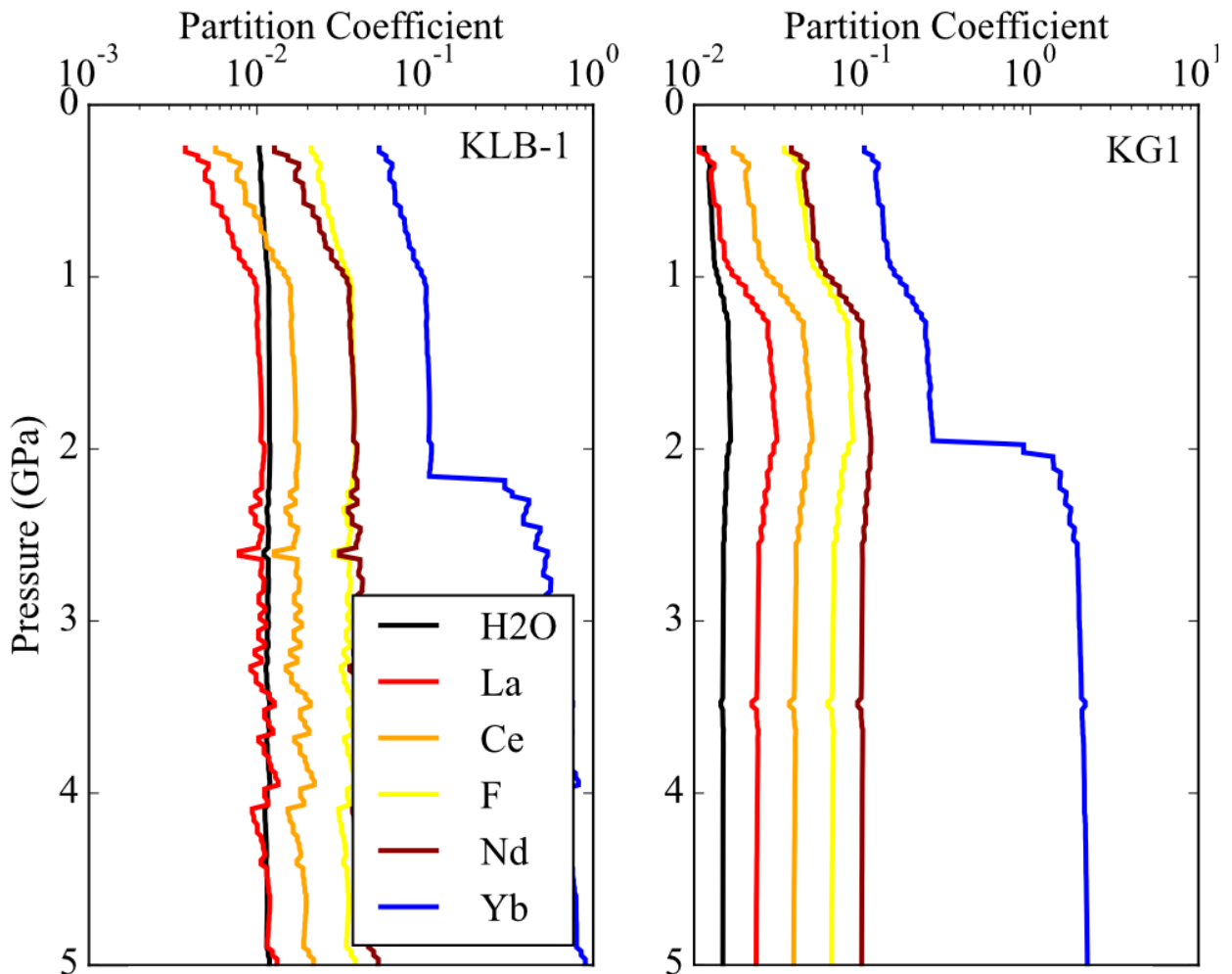


Figure S9. Partition coefficients predicted for key volatile and non-volatile trace elements during mantle melting.

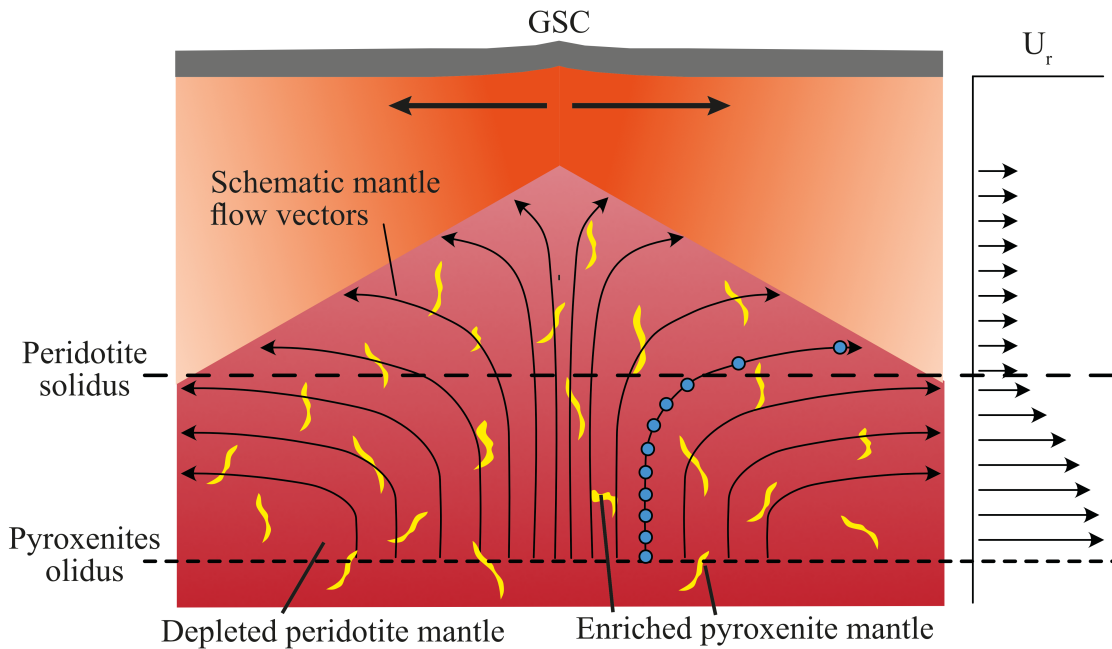


Figure S10. Schematic of the geometry of melting beneath the ridge. A qualitative description of the relative mantle flow velocity of material exciting the melting region is displayed on the right hand side. The increased velocity below the anhydrous peridotite solidus is caused by buoyant upwelling of plume-material. Blue circles demonstrate the locations at which melt compositions are calculated for one region of mantle (i.e. melt calculated at set pressures along a single mantle flow path).

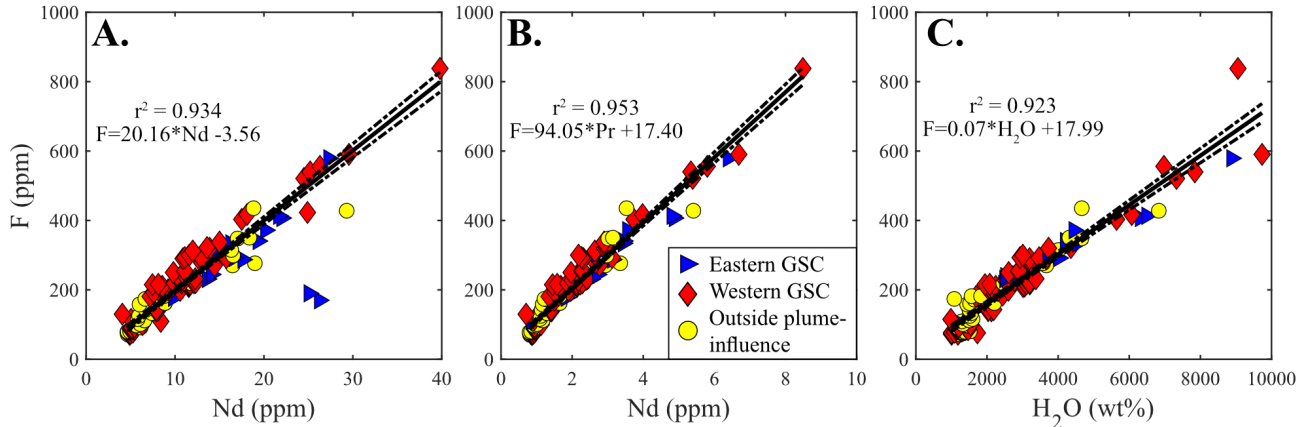


Figure S11. Relationship between F and other incompatible trace elements Nd, Pr and H_2O .

Data is from this study (Supplementary Excel file) and that of Ingle et al. (2010) and Le Voyer et al. (2019). The two eastern GSC samples with anomalously low F concentrations are found at $\sim 85.8^\circ W$, near an oceanic transform fault and at the margin of plume influence (data from Le Voyer et al. (2019)). Strong correlations are seen between F and Nd or Pr, indicating similar compatibilities to these trace elements during mantle melting. The data displayed here has not been corrected for the influence of fractional crystallisation and brine assimilation.

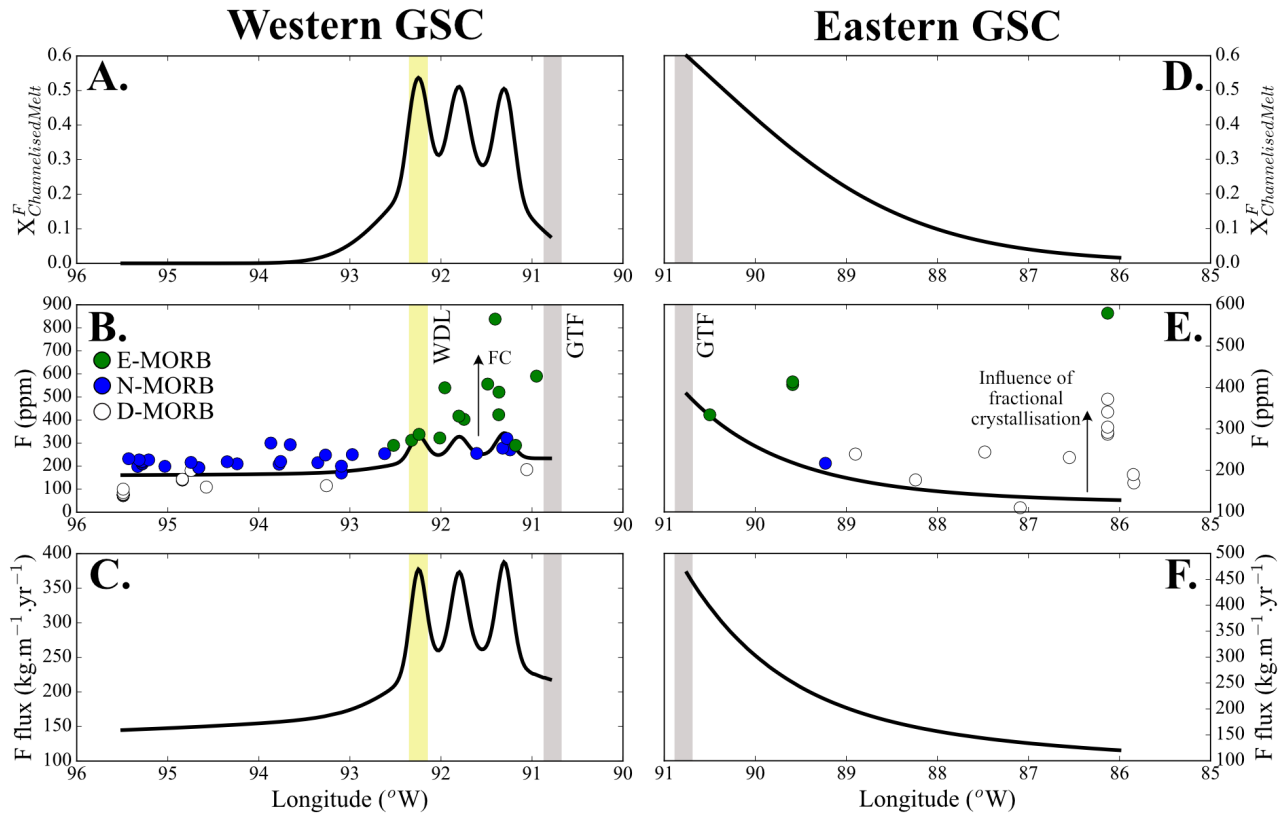


Figure S12. Longitudinal variation in the flux and concentration of F predicted by 2-component mantle melting models that account for 2-phase flow between the Galápagos mantle plume and GSC. Models shown here are identical to those presented in figures 5 and 9 of the main text. Results for the western and eastern GSC are shown in panels **A. - C.** and **D. - F.**, respectively. **A., D.** the fraction of F sourced from channelised melts (X_F), which reaches $\sim 50\%$ in the regions of greatest plume influence. **B., E.**, concentration of F predicted by our mantle melting models against the measured F contents of the GSC basalts. Our model predictions bracket the lower end of the available F data, which has not been corrected for the influence of fractional crystallisation. **C., F.** the flux of F from the GSC is greatest in the regions of strongest plume influence.

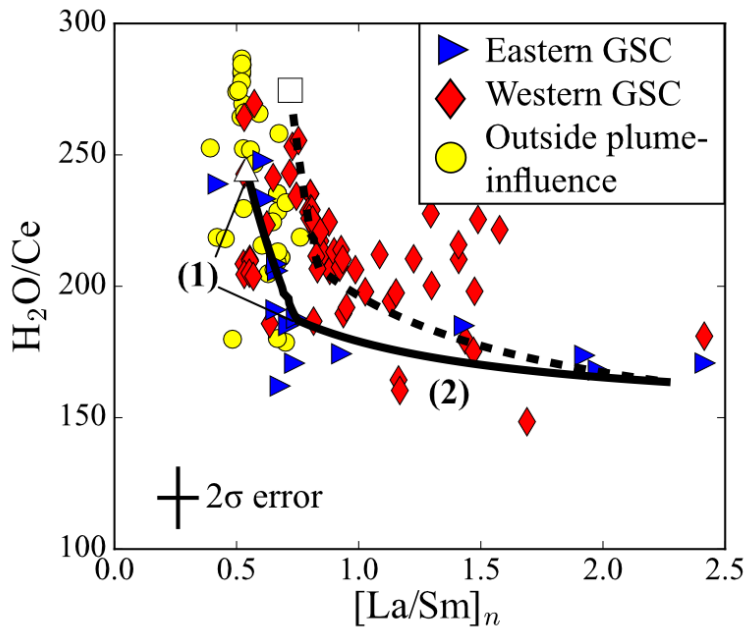


Figure S13. Relationship between H_2O/Ce and $[La/Sm]_n$ in the GSC basalts. The black lines represent the model results for melting beneath the eastern (solid line) and western (dashed line) GSC with an increasing contribution of plume-derived channelised flow. The models displayed here are identical to those seen in Fig. 2 of the main text. The H_2O contents of the various mantle sources are: 100 ppm for the eastern GSC peridotite, 145 ppm for the western GSC peridotite, and 550 ppm for the pyroxenite source component. Region **1** represents an increasing fraction of pyroxenite in the sub-ridge mantle (up to 8%), and region **2** represents an increase in the fraction of channelised melt (where the pressure of channel formation is 3.3 GPa). This diagram shows that our estimates for the H_2O contents of the various mantle components can recreate the H_2O/Ce ratio of the GSC basalts as well as their H_2O/La ratios.

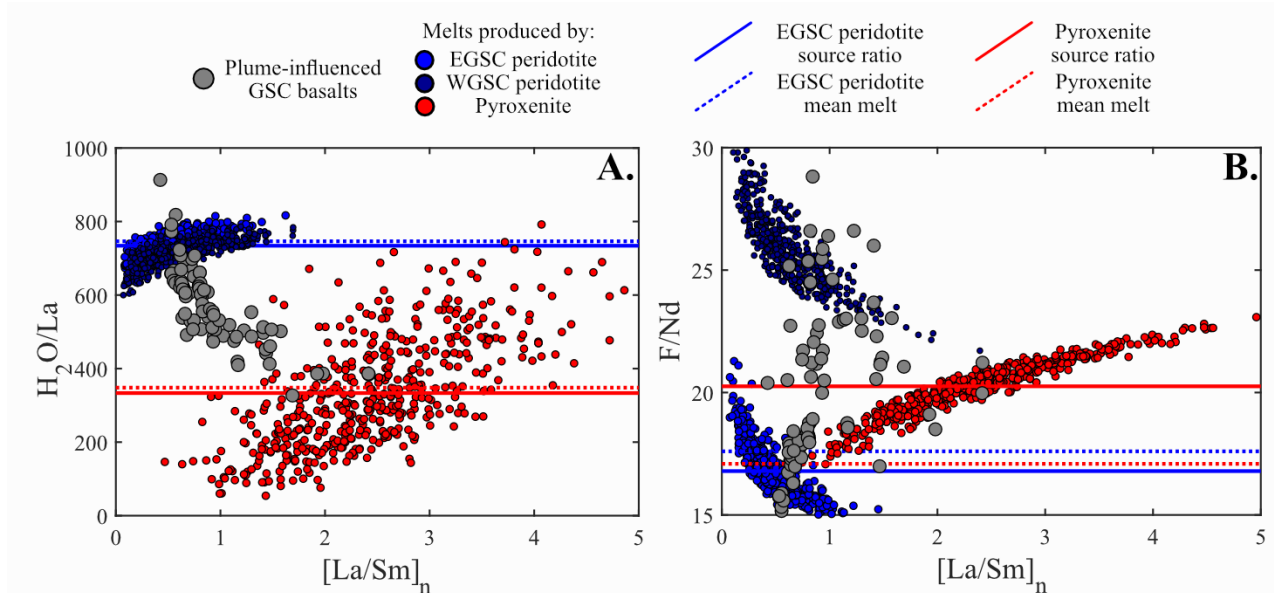


Figure S14. Comparison of the trends produced in H_{2O}/La vs $[La/Sm]_n$ and F/Nd vs $[La/Sm]_n$ space by mantle melting of a single mantle component versus the trend observed in the GSC plume-influenced basalts (shown in grey). Blue symbols represent the melts produced by melting of a peridotite source component beneath the eastern (light blue) and western (dark blue) GSC. Red symbols represent the melts produced by melting of a pyroxenitic mantle component. Melt compositions are calculated by taking the instantaneous melts formed at each step of the melting calculations and allowing very small amounts of mixing to occur (using a Dirichlet mixing function; Rudge et al. (2013)). We can see that the melting models predict a positive correlation between H_{2O}/La and $[La/Sm]_n$ for both lithologies, opposite to the trends observed in the GSC basalts.

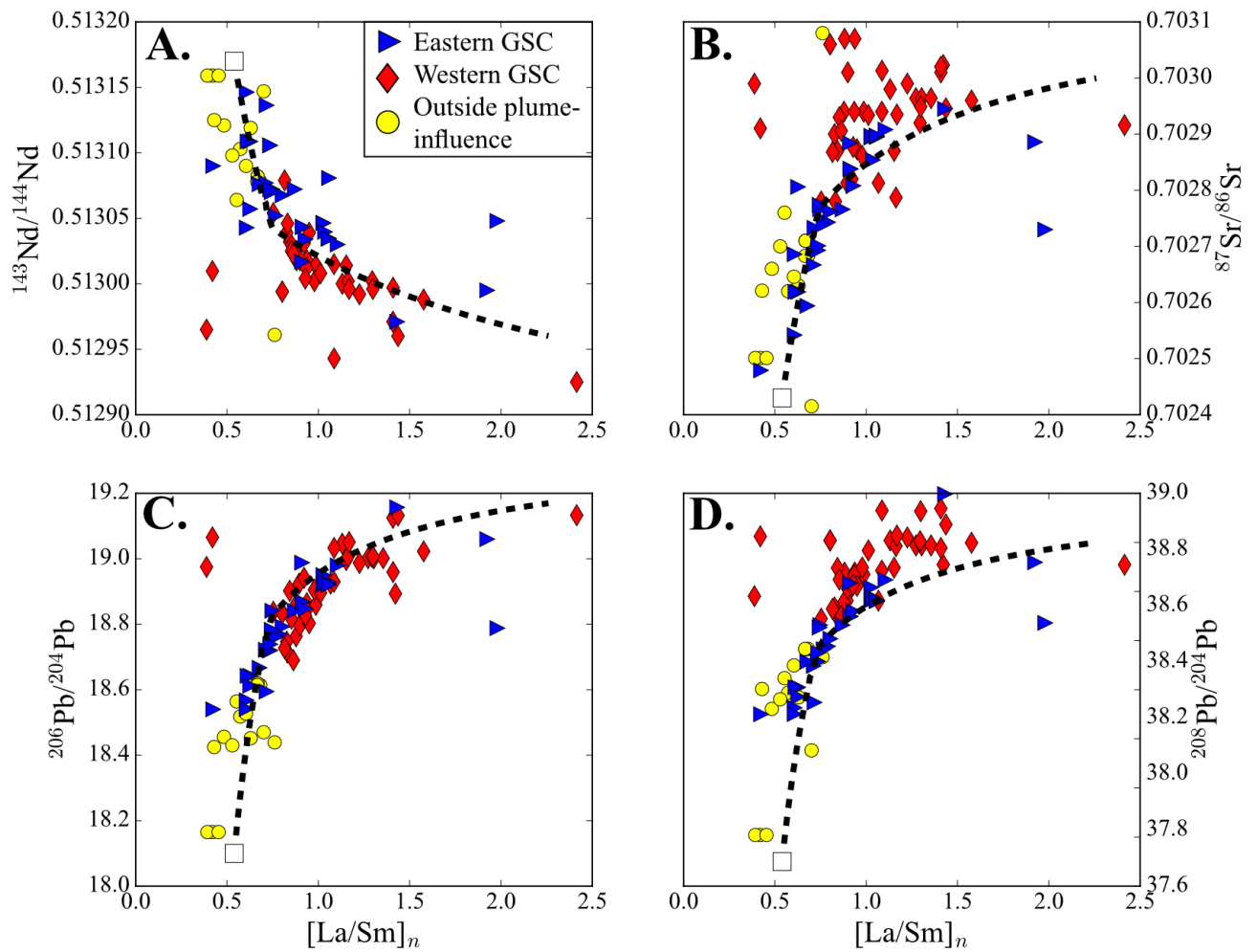


Figure S15. Isotopic composition predicted by our mantle melting models (models are identical to those shown in Fig. 2 of the main text and Fig. S13 here). Notably, the composition of the GSC basalts can be produced when the isotopic composition of the enriched (pyroxenitic) endmember are set at: $^{87}\text{Sr}/^{86}\text{Sr} = 0.7030$, $^{143}\text{Nd}/^{144}\text{Nd} = 0.51296$, $^{206}\text{Pb}/^{204}\text{Pb} = 19.17$, $^{208}\text{Pb}/^{204}\text{Pb} = 38.8$. The isotopic composition of the depleted mantle components are set using the values estimated by Harpp and White (2001). The Sr, Pb and Nd concentration of the enriched mantle source are 52.1, 0.18, and 3.97 ppm, respectively.